

A Novel Shape Estimation Strategy for Continuum Robots Using Multiple Hall-effect Sensors and IMUs

Yehui Li¹, Yujing Kuang¹, Mingyue Cui^{2,1} [✉], and Weibing Li¹

¹ School of Computer Science and Engineering, Sun Yat-sen University, Guangzhou 510006, China

liyh699@mail.sysu.edu.cn; kuangyj8@mail2.sysu.edu.cn;
liwb53@mail.sysu.edu.cn

² Engineering Research Center of Software/Hardware Co-design Technology and Application, Ministry of Education (East China Normal University), China
cuimy5@mail.sysu.edu.cn

Abstract. Accurate real-time shape estimation is critical for continuum robots in applications such as minimally invasive surgery and confined-space exploration. Existing methods often rely on costly or impractical sensing technologies. This paper proposes a novel real-time, low-cost, high-accuracy shape estimation strategy that fuses data from embedded Hall-effect sensors and inertial measurement units (IMUs). The system employs an annular magnet at the base of the continuum robot and three sensor modules to measure magnetic fields and orientations. An optimization framework based on the fusion of magnetic field data and orientation data measured by the sensor module is developed for sensor positioning, while three curve-fitting methods, including piecewise quadratic Bezier, cubic Bezier, and Kasa least-squares circular arc, are developed for shape reconstruction. Experimental validation is conducted on a physical continuum robot platform, demonstrating that the proposed strategy combining the sensor positioning method and the Kasa least-squares circular-arc fitting method can achieve accurate shape estimation for the developed continuum robot, with an average error of less than 1 mm and a real-time frequency of 25 Hz.

Keywords: Continuum robots · Shape estimation · Multi-sensor fusion.

* This work was supported in part by the Sun Yat-sen University Training Program of Innovation and Entrepreneurship for Undergraduates Under Grant 20251122, in part by the Open Project Program for the Engineering Research Center of Software/Hardware Co-design Technology and Application, Ministry of Education (East China Normal University), Grant No. 67000-42990016, in part by the National Natural Science Foundation of China under Grant 62206317, in part by the Guangxi Key Research and Development Project under Grant 2024AB08049, and in part by the Guangzhou Basic and Applied Basic Research Foundation under Grant 2025A04J5280. (Corresponding author: Mingyue Cui)

1 Introduction

Continuum robots, renowned for their high dexterity and adaptability, are increasingly vital in applications like minimally invasive surgery [1–3], industrial inspection in confined spaces [4], and hazardous environment exploration [5]. Unlike rigid-link robots, their ability to conform to complex geometries and navigate narrow passages makes them ideal for delicate manipulation in unstructured environments. Accurate real-time shape estimation is essential for precise control and safe interaction. However, complex deformations arising from nonlinear elasticity, hysteresis, friction, and external forces make direct shape measurement of continuum robots challenging.

There are various model-based approaches for continuum robots that leverage kinematic formulations and mechanical models to theoretically reconstruct shape without physical sensors [6–8]. However, these methods exhibit fundamental limitations when deployed in practical scenarios, as their accuracy deteriorates under unmodeled dynamic effects, including material nonlinearity, hysteresis phenomena, complex friction distributions, and unpredictable environmental interactions (particularly tissue contact forces in biological applications). This inherent vulnerability to real-world disturbances has motivated significant research toward sensor-based solutions. Consequently, contemporary approaches increasingly employ multi-modal sensing frameworks integrated with advanced reconstruction algorithms to achieve reliable shape estimation [9]. External sensing methodologies represent a well-established category that directly monitors either the robot’s global geometry or discrete marker positions attached to its structure, such as optical tracking [10], electromagnetic (EM) tracking [11], vision tracking [12], ultrasound image processing [13], and fluoroscopic X-ray imaging [14]. While achieving remarkable spatial precision (often less than 1 mm absolute positioning accuracy), these solutions impose substantial operational constraints through their dependence on complex and expensive peripheral hardware. Computer vision implementations, for instance, become fundamentally inapplicable in endoscopic or intracorporeal surgical contexts due to insurmountable line-of-sight limitations, while EM systems suffer critical field distortion in metallic environments. Such restrictions severely curtail their deployment in precisely the applications where continuum robots demonstrate greatest utility.

In contrast to external sensing paradigms, embedded sensors directly measure intrinsic physical properties through transducers integrated within the robot’s structural body, eliminating dependency on proximal monitoring hardware. Such sensors include fiber optic sensors detecting strain via light propagation changes [15], fiber Bragg grating (FBG) arrays capturing distributed curvature through strain-induced wavelength shifts [16,17], inertial measurement units (IMUs) providing high-frequency orientation data [18–20], Hall-effect sensors quantifying magnetic field vectors [21, 22], and compliant electronics enabling stretchable conformal sensing [23]. The absence of external infrastructure significantly expands operational envelopes, particularly in confined or occluded environments like surgical cavities and industrial piping systems, unlocking applications inaccessible to external sensing counterparts [24]. While FBG technology achieves

exceptional spatial resolution (sub-millimeter curvature sampling along >250 mm lengths), its adoption remains constrained by substantial costs. While shape estimation methods employing IMUs or Hall-effect sensors remain low cost, currently, existing implementations of these methods often solely rely on one type of sensor, which results in insufficient accuracy and limits their practical utility.

To overcome these limitations, we propose a novel real-time, low-cost shape estimation strategy that synergistically combines magnetic field sensing with IMU-based orientation measurements. Our system features an annular magnet placed at the base of the continuum robot and three sensor modules equidistantly embedded inside the continuum body. Each module features co-located IMU and Hall-effect sensors for simultaneous attitude measurement and magnetic field detection. Through multi-modal data fusion, we reconstruct the precise position and orientation of each module. We subsequently evaluate three curve-fitting methods, three curve-fitting methods, including the piecewise quadratic Bezier curve fitting, the cubic Bezier curve fitting, and the Kasa least-squares circular arc fitting, for shape estimation of the continuum robot. Experimental validation is comprehensively conducted, with the results demonstrating that the proposed shape estimation strategy combining the sensor position method and the Kasa least-squares circular arc fitting method can achieve real-time and accurate shape estimation of the continuum robot, with an average error of less than 1 mm and a maximum error of less than 3 mm. For better understanding, the main contributions of this work are summarized as follows:

- 1) A novel real-time, low-cost, and high-accuracy shape estimation strategy for continuum robots is proposed, which combines magnetic field sensing and IMU-based orientation measurement.
- 2) A novel sensor positioning method by fusing the Hall-effect sensor data and IMU data is proposed, based on which three curve-fitting methods are developed for shape estimation for continuum robots.
- 3) Experimental validation is comprehensively conducted on a physical continuum robot platform, demonstrating the effectiveness and sub-millimeter precision of the proposed shape estimation strategy.

2 Method

This section first presents an overview of the proposed continuum robot with shape sensing capability. Subsequently, a novel positioning strategy leveraging multiple Hall-effect sensors and inertial measurement units (IMUs) is introduced to accurately obtain the spatial pose of targeted segments along the continuum robot. Finally, several advanced curve-fitting techniques are developed to reconstruct the continuum robot's three-dimensional shape.

2.1 System Overview

As shown in Fig.1, with a length of 100 mm and a diameter of 14 mm, the developed continuum robot is mainly composed of an axial-magnetized annular

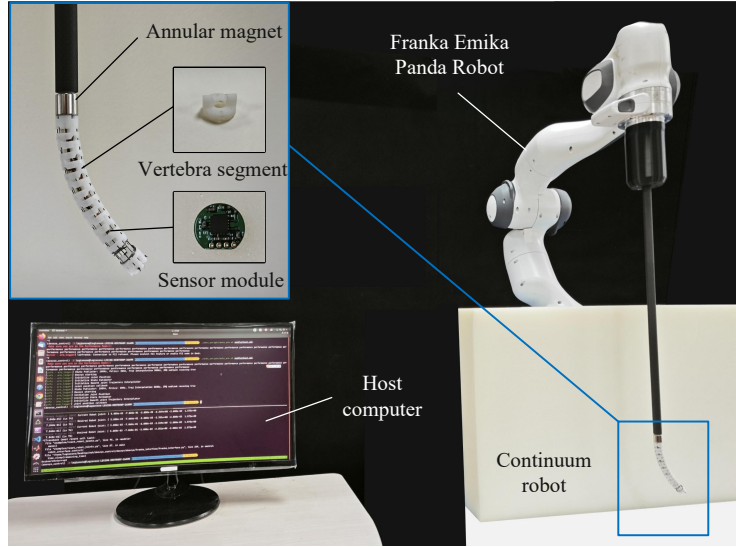


Fig. 1. Overview and components of the developed continuum robot with shape estimation capability.

permanent magnet (length: 13 mm, inner diameter: 10 mm, outer diameter: 14 mm, NdFeB N52), several 3D-printed vertebra segments, and three sensor modules. Each sensor module is composed of a Hall-effect sensor (MLX90393) on one side and an IMU (MPU6050) on the other side. These sensor modules are embedded inside the vertebra segments with an interval of 25 mm, which are connected to a microcontroller (Arduino Nano) via the I2C bus. Four cables passing through each segment are connected to two servo motors (Waveshare ST3215 Servo controlled by the microcontroller) and utilized for bending control of the continuum robot. The continuum robot is attached to a carbon fiber tube and mounted on a robot arm (Franka Emika Panda robot), with which dexterous manipulation of the continuum robot can be performed.

2.2 Sensor Positioning

This subsection details the proposed positioning strategy for obtaining the pose of three sensor modules embedded inside the continuum robot. As shown in Fig. 2, four coordinate frames of the developed continuum robot are defined, while the world coordinate frame $\{O_W\}$ is fixed at the robot arm base.

Magnetic field modeling: Typically, the magnetic moment magnitude M_c of a permanent magnet depends on its volume and magnetization strength, which should be a constant for a given magnet with a specific size and grade. Since the continuum robot is mounted on a robot arm, based on forward kinematics analysis of the system, one can easily obtain the rotation matrix $\mathbf{R}_0^W = [\mathbf{r}_x \ \mathbf{r}_y \ \mathbf{r}_z] \in$

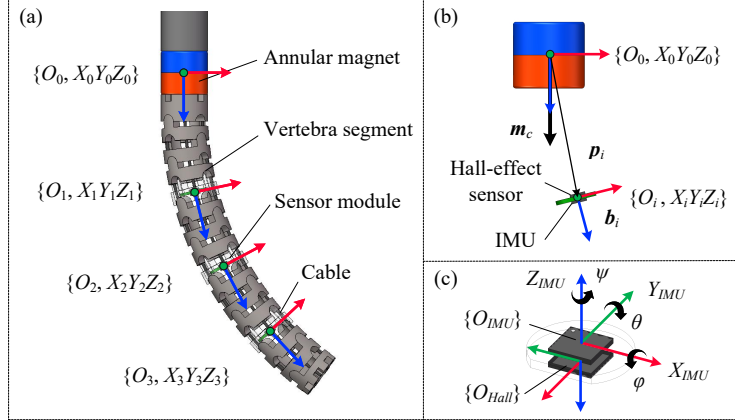


Fig. 2. Detailed illustration of the developed continuum robot. (a) Coordinate frames of the continuum robot. (b) Illustration of modeling the generated magnetic field at the i -th sensor module using the magnetic dipole model. (c) Coordinate frames of the sensor module.

$\mathbb{R}^{3 \times 3}$ between the world frame and the magnet frame as well as the magnet position $\mathbf{p}_0 \in \mathbb{R}^{3 \times 1}$ with respect to the world frame. Then, one can obtain the magnetic moment vector of the given magnet as

$$\mathbf{m}_c = \mathbf{r}_z M_c \in \mathbb{R}^{3 \times 1}. \quad (1)$$

For a permanent magnet with a known magnetic moment \mathbf{m}_c , as shown in Fig. 2(b), the generated magnetic field at the position of the i -th sensor module can be calculated by employing the famous magnetic dipole model as [25]

$$\mathbf{b}_i^{\text{model}} = \frac{\mu_0}{4\pi \|\mathbf{p}_i\|^3} \left(3\hat{\mathbf{p}}_i \hat{\mathbf{p}}_i^\top - \mathbf{I} \right) \mathbf{m}_c \in \mathbb{R}^{3 \times 1} \quad (2)$$

where μ_0 is the magnetic permeability of free space; $\mathbf{p}_i = \mathbf{p}_{Si} - \mathbf{p}_0 \in \mathbb{R}^{3 \times 1}$ is the displacement vector from the annular magnet \mathbf{p}_0 to the i -th sensor module \mathbf{p}_{Si} ; $\hat{\mathbf{p}}_i$ is the normalized vector of \mathbf{p}_i (i.e., $\mathbf{p}_i \|\mathbf{p}_i\|^{-1}$); \mathbf{I} is a 3×3 identity matrix.

Magnetic field measurement: The IMU embedded inside the sensor module contains an accelerometer and a gyroscope. Assuming in the initial state, the continuum robot is straight with the magnetic moment \mathbf{m}_c aligned with the gravitational acceleration, which means that the initial acceleration \mathbf{a} measured is equal to the gravitational acceleration. When the continuum robot is controlled to be a new specific pose, the gravitational acceleration will produce corresponding components on the three axes of the accelerometer, with the measured acceleration $\mathbf{a} = [a_x \ a_y \ a_z]^\top$. Then, one can easily obtain the following

angles as

$$\theta_{acc} = \arctan\left(\frac{a_y}{a_z}\right), \quad \varphi_{acc} = \arctan\left(\frac{a_x}{\sqrt{a_y^2 + a_z^2}}\right) \quad (3)$$

where θ_{acc} and φ_{acc} are the calculated roll and pitch angles based on the acceleration \mathbf{a} measured by the accelerometer, respectively. Since the rotation around the gravitational axis will not lead to any change of the measured acceleration \mathbf{a} , the yaw angle ψ cannot be calculated directly by the accelerometer, which can only be obtained by gyroscope integration.

With the angular velocity $\mathbf{g} = [g_x \ g_y \ g_z]^\top$ (around the three axes of the gyroscope) measured by the gyroscope, the changing rate $\boldsymbol{\omega}$ of the Euler angles can be calculated as

$$\begin{bmatrix} \omega_\theta \\ \omega_\varphi \\ \omega_\psi \end{bmatrix} = \begin{bmatrix} 1 & \frac{\sin \varphi \sin \theta}{\cos \varphi} & \frac{\cos \theta \sin \varphi}{\cos \varphi} \\ 0 & \cos \theta & -\sin \theta \\ 0 & \frac{\sin \theta}{\cos \varphi} & \frac{\cos \theta}{\cos \varphi} \end{bmatrix} \begin{bmatrix} g_x \\ g_y \\ g_z \end{bmatrix} \quad (4)$$

where ω_θ , ω_φ , and ω_ψ are components of the Euler angles' changing rate $\boldsymbol{\omega}$. Then, a first-order complementary filter is employed that blends the Euler angles in (3) with the high-frequency gyroscope integration, which thus obtains the updated Euler angles at time k as

$$\begin{bmatrix} \theta_k \\ \varphi_k \\ \psi_k \end{bmatrix} = \alpha \left(\begin{bmatrix} \theta_{k-1} \\ \varphi_{k-1} \\ \psi_{k-1} \end{bmatrix} + \begin{bmatrix} \omega_\theta \\ \omega_\varphi \\ \omega_\psi \end{bmatrix} \Delta t \right) + (1 - \alpha) \begin{bmatrix} \theta_{acc} \\ \varphi_{acc} \\ \psi_{acc} \end{bmatrix} \quad (5)$$

where α is a weighted parameter ($\alpha = 0.2$ in this work, indicating that the update of Euler angles depends more on the accelerometer); $\Delta t = 0.01$ s denotes the sampling time. The Euler angles at the initial state can be obtained by only using the accelerometer, with the initial yaw angle set as zero. After that, the resultant Euler angles can be converted into a unit quaternion \mathbf{q} as

$$\mathbf{q} = \begin{bmatrix} q_0 \\ q_1 \\ q_2 \\ q_3 \end{bmatrix} = \begin{bmatrix} \cos(\varphi/2) \cos(\theta/2) \cos(\psi/2) + \sin(\varphi/2) \sin(\theta/2) \sin(\psi/2) \\ \sin(\varphi/2) \cos(\theta/2) \cos(\psi/2) - \cos(\varphi/2) \sin(\theta/2) \sin(\psi/2) \\ \cos(\varphi/2) \sin(\theta/2) \cos(\psi/2) + \sin(\varphi/2) \cos(\theta/2) \sin(\psi/2) \\ \cos(\varphi/2) \cos(\theta/2) \sin(\psi/2) - \sin(\varphi/2) \sin(\theta/2) \cos(\psi/2) \end{bmatrix}. \quad (6)$$

Based on the resultant quaternion \mathbf{q} , one can naturally calculate the rotation matrix \mathbf{R}_S^W between the world frame and the i -th sensor frame as

$$\mathbf{R}_{Si}^W = \begin{bmatrix} q_0^2 + q_1^2 - q_2^2 - q_3^2 & 2(q_1 q_2 - q_0 q_3) & 2(q_1 q_3 + q_0 q_2) \\ 2(q_1 q_2 + q_0 q_3) & q_0^2 - q_1^2 + q_2^2 - q_3^2 & 2(q_2 q_3 - q_0 q_1) \\ 2(q_1 q_3 - q_0 q_2) & 2(q_2 q_3 + q_0 q_1) & q_0^2 - q_1^2 - q_2^2 + q_3^2 \end{bmatrix} \in \mathbb{R}^{3 \times 3}. \quad (7)$$

As shown in Fig. 2(c), the coordinate of the IMU embedded inside the i -th sensor module is the same as the sensor's coordinate, while the coordinate of the Hall-effect sensor is different from that of the IMU (the small translation (less than 0.2 mm) between two origins can be neglected.) Consequently, the rotation matrix between the world frame and the i -th Hall-effect sensor frame is calculated as

$$\mathbf{R}_{Hi}^W = \mathbf{R}_{Si}^W \mathbf{R}_{Hi}^{Si}, \text{ with } \mathbf{R}_{Hi}^{Si} = \begin{bmatrix} 0 & -1 & 0 \\ -1 & 0 & 0 \\ 0 & 0 & -1 \end{bmatrix}. \quad (8)$$

By noting that the magnetic field \mathbf{b}_i^{Hi} measured by the i -th Hall-effect sensor is represented in its coordinate frame, the transformed magnetic field \mathbf{b}_i^W represented in the world coordinate frame can be calculated as

$$\mathbf{b}_i^W = \mathbf{R}_{Hi}^W \mathbf{b}_i^{Hi}. \quad (9)$$

Optimization formulation and solving: With the modeled magnetic field $\mathbf{b}_i^{\text{model}}$ and the measured magnetic field \mathbf{b}_i^W , one can formulate an optimization to obtain the position of the i -th sensor module as

$$\begin{aligned} \arg \min_{\mathbf{p}_{Si}} \quad & \|\mathbf{b}_i^W - \mathbf{b}_i^{\text{model}}(\mathbf{p}_{Si})\|_2^2 \\ \text{s. t.} \quad & \mathbf{p}_{Si}^- \preceq \mathbf{p}_{Si} \preceq \mathbf{p}_{Si}^+ \end{aligned} \quad (10)$$

where $\|\cdot\|_2$ is the 2-norm; \mathbf{p}_{Si}^- and \mathbf{p}_{Si}^+ are the lower and upper boundary of the i -th sensor's position \mathbf{p}_{Si} , respectively; \preceq is an element-wise (general) inequality symbol. In this work, the formulated optimization problem is solved by using the *fmincon* function built in MATLAB, with the *Algorithm* option selected as '*interior-point*'. The average processing time for an individual optimization problem is around 9 ms, with an overall processing time of less than 30 ms for calculating three sensor positions.

2.3 Curve Fitting

This subsection details three curve fitting methods based on the obtained sensor positions and orientations, which thus achieve shape estimation of the developed continuum robot.

Piecewise quadratic Bezier curve: Given the control points $\mathbf{p}_0, \mathbf{p}_1, \dots, \mathbf{p}_n$, a Bezier curve with these control points is given by

$$\mathcal{P}(t) = \mathcal{B}_0^n(t)\mathbf{p}_0 + \mathcal{B}_1^n(t)\mathbf{p}_1 + \dots + \mathcal{B}_n^n(t)\mathbf{p}_n = \sum_{k=0}^n \mathcal{B}_k^n(t)\mathbf{p}_k \quad (11)$$

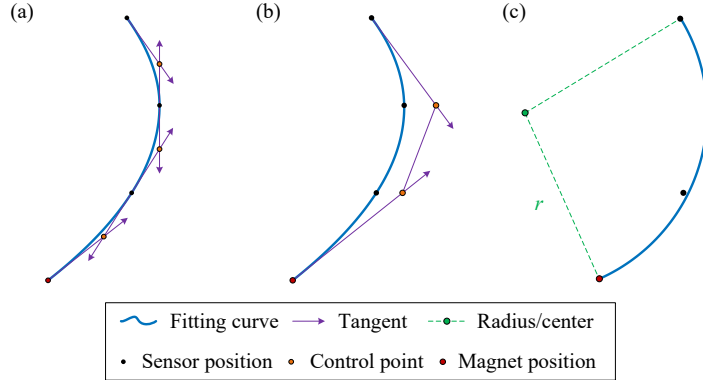


Fig. 3. Curve fitting using different methods. (a) Piecewise quadratic Bezier curve fitting. (b) Cubic Bezier curve fitting. (c) Circular-arc curve fitting.

where t is a parameter that varies between 0 and 1, controlling the position along the curve; $\mathcal{B}_k^n(t)$ is the blending function, which is defined as

$$\mathcal{B}_k^n(t) = \mathcal{C}(n, k)t^k(1-t)^{n-k}$$

with $\mathcal{C}(n, k) = \frac{n!}{k!(n-k)!}$ as the binomial coefficient. A Bezier curve always passes through its first and last control points [26].

With the obtained magnet position \mathbf{p}_0 and three sensor positions $\mathbf{p}_i (i = 1, 2, 3)$, a piecewise quadratic Bezier curve is employed to estimate the shape of the continuum robot. The illustration of a piecewise quadratic Bezier curve is shown in Fig. 3(a). Firstly, both the position and orientation of the magnet and sensor are projected onto the $r - z$ plane as

$$\bar{\mathbf{p}}_i = \begin{bmatrix} \sqrt{p_{xi}^2 + p_{yi}^2} \\ p_{zi} \end{bmatrix}, \quad \bar{\mathbf{n}}_i = \begin{bmatrix} \sqrt{n_{xi}^2 + n_{yi}^2} \\ n_{zi} \end{bmatrix}. \quad (12)$$

where $\bar{\mathbf{n}}_i$ is the orientation of the i -th sensor, which can be obtained by extracting the z element of the rotation matrix \mathbf{R}_i^W . Then, a quadratic Bezier curve is constructed to connect the two adjacent converted points as

$$\mathcal{P}_i^{i+1}(t) = (1-t)^2\bar{\mathbf{p}}_i + 2(1-t)t\beta_i + t^2\bar{\mathbf{p}}_{i+1} \quad (13)$$

where $\beta_i \in \mathbb{R}^{2 \times 1}$ is the constructed control point for the quadratic Bezier curve \mathcal{P}_i^{i+1} , which determine the shape of the fitting curve as well as the smoothness between two adjacent curves. In this work, the control point β_i is selected as the intersection of the two projected orientations $\bar{\mathbf{n}}_i$ and $-\bar{\mathbf{n}}_{i+1}$, which indicates that both $\bar{\mathbf{n}}_i$ and $-\bar{\mathbf{n}}_{i+1}$ become the tangent of the construct Bezier curve. The control point β_i is calculated as

$$\beta_i = \bar{\mathbf{p}}_i + \kappa\bar{\mathbf{n}}_i \quad (14)$$

where the parameter

$$\kappa = \frac{\det [\bar{\mathbf{n}}_{i+1} \quad (\bar{\mathbf{p}}_{i+1} - \bar{\mathbf{p}}_i)]}{\det [\bar{\mathbf{n}}_i \quad \bar{\mathbf{n}}_{i+1}]}.$$

By constructing the quadratic Bezier curve subsequently, one can finally obtain a continuous and smooth curve for shape estimation of the continuum robot.

Cubic Bezier curve: A single cubic Bezier curve passing through four prescribed points $\bar{\mathbf{p}}_i$ ($i = 0, 1, 2, 3$) is constructed, as shown in Fig. 3(b), with the continuity and smoothness across the whole segment guaranteed. The constructed Bezier curve is expressed as

$$\mathcal{P}(t) = (1-t)^3 \bar{\mathbf{p}}_0 + 3(1-t)^2 t \beta_1 + 3(1-t)t^2 \beta_2 + t^3 \bar{\mathbf{p}}_3 \quad (15)$$

where the unknown internal control points β_1 and β_2 are determined by enforcing interpolation at two parametric positions $t_1 = 1/3$ and $t_2 = 2/3$. Specifically, the control points β_1 and β_2 are calculated as

$$\begin{bmatrix} \beta_1 \\ \beta_2 \end{bmatrix} = \mathcal{A}^{-1} \zeta \in \mathbb{R}^{4 \times 1} \quad (16)$$

where

$$\mathcal{A} = \begin{bmatrix} 3(1-t_1)^2 t_1 & 3(1-t_1)t_1^2 \\ 3(1-t_2)^2 t_2 & 3(1-t_2)t_2^2 \end{bmatrix} \in \mathbb{R}^{4 \times 4}, \quad \zeta = \begin{bmatrix} \bar{\mathbf{p}}_1 - (1-t_1)^3 \bar{\mathbf{p}}_0 - t_1^3 \bar{\mathbf{p}}_3 \\ \bar{\mathbf{p}}_2 - (1-t_2)^3 \bar{\mathbf{p}}_0 - t_2^3 \bar{\mathbf{p}}_3 \end{bmatrix} \in \mathbb{R}^4$$

are used for calculation of the two control points' positions.

Circular-arc curve: Assuming the four projected points lie on a common circular arc with a constant curvature, as shown in Fig. 3(c), the Kasa least-squares circle [27] is employed to reconstruct the shape of the continuum robot. The circle center $\mathbf{c} = [x_c, y_c]^\top$ and radius r of the fitting circular-arc curve are determined based on the projected points.

For these projected points $\bar{\mathbf{p}}_i = [x_i, y_i]^\top$, there would be an optimal fitting circle satisfies

$$(x_i - x_c)^2 + (y_i - y_c)^2 = r^2 \quad (17)$$

where $\mathbf{c} = [x_c, y_c]^\top$ and r are the center and radius of the fitting circle, respectively. By expanding (17), one can have

$$2x_i x_c + t y_i y_c + \sigma = x_i^2 + y_i^2 \quad (18)$$

where $\sigma = r^2 - x_c^2 - y_c^2$. By substituting the four projected points into (18), one can have

$$\mathcal{D}\delta = \eta \quad (19)$$

where

$$\mathcal{D} = \begin{bmatrix} 2x_1 & 2y_1 & 1 \\ \vdots & \vdots & \vdots \\ 2x_4 & 2y_4 & 1 \end{bmatrix} \in \mathbb{R}^{4 \times 3}, \quad \boldsymbol{\delta} = \begin{bmatrix} x_c \\ y_c \\ \sigma \end{bmatrix} \in \mathbb{R}^{3 \times 1}, \quad \boldsymbol{\eta} = \begin{bmatrix} x_1^2 + y_1^2 \\ \vdots \\ x_4^2 + y_4^2 \end{bmatrix} \in \mathbb{R}^{4 \times 1}.$$

Then, the least-squares solution can be expressed as

$$\boldsymbol{\delta} = \begin{bmatrix} x_c \\ y_c \\ \sigma \end{bmatrix} = (\mathcal{D}^\top \mathcal{D})^{-1} \mathcal{D}^\top \boldsymbol{\eta}, \quad \text{and } r = \sqrt{x_c^2 + y_c^2 + \sigma}. \quad (20)$$

Let the polar angle of each point be $\vartheta_i = \arctan\left(\frac{y_i - y_c}{x_i - x_c}\right)$, with $i = 0, 1, 2, 3$.

By choosing the direction $\varrho = 1$ (counter-clockwise) or $\varrho = -1$ (clockwise) such that two intermediate angles ϑ_1, ϑ_2 lie between ϑ_0 and ϑ_3 along the selected orientation, more angles can be interpolated as

$$\vartheta(t) = \vartheta_0 + \varrho|\vartheta_3 - \vartheta_0|t, \quad 0 \leq t \leq 1 \quad (21)$$

where $\vartheta(t)$ is the interpolating angle between ϑ_0 and ϑ_3 . Finally, one can obtain the circular-arc fitting curve as

$$\mathcal{P}(t) = \begin{bmatrix} x_c + r \cos(\vartheta(t)) \\ y_c + r \sin(\vartheta(t)) \end{bmatrix}, \quad 0 \leq t \leq 1. \quad (22)$$

It should be noted that the constructed fitting curves mentioned above are projected onto the $r - z$ plane, to recover the 3D shape of the continuum robot, each point $\mathcal{P}_j = [\mathcal{P}_{rj}, \mathcal{P}_{zj}]^\top$ on the fitting curve needs to convert to

$$\tilde{\mathcal{P}}_j = \begin{bmatrix} \tilde{\mathcal{P}}_{xj} \\ \tilde{\mathcal{P}}_{yj} \\ \tilde{\mathcal{P}}_{zj} \end{bmatrix} = \begin{bmatrix} \wp_x \mathcal{P}_{rj} \\ \wp_y \mathcal{P}_{rj} \\ \mathcal{P}_{zj} \end{bmatrix} \quad (23)$$

where

$$\wp_x = \frac{\sum_{i=0}^4 p_{xi}}{\sum_{i=0}^4 \sqrt{p_{xi}^2 + p_{yi}^2}}, \quad \wp_y = \frac{\sum_{i=0}^4 p_{yi}}{\sum_{i=0}^4 \sqrt{p_{xi}^2 + p_{yi}^2}} \quad (24)$$

are two parameters for determining the component proportions in the x and y axes, respectively.

3 Experimental Validation

In this section, a fixed curvature test is conducted on a bending curvature template to validate the effectiveness and efficacy of the proposed shape estimation strategy for the developed continuum robot. As shown in Fig. 4, the template

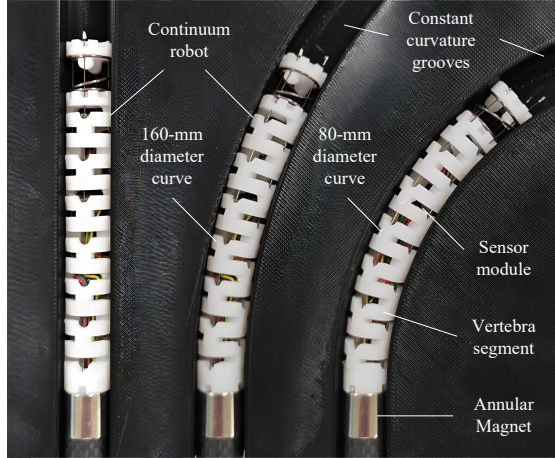


Fig. 4. Experimental setup for evaluating the effectiveness and efficacy of the proposed shape estimation strategy by placing the continuum robot into a 3D-printed bending curvature template.

is 3D printed with fixed curvature grooves of 14.2 mm, which is approximately equal to the outer diameter of the continuum robot. There are three grooves inside the template, with one as a straight groove and the others as constant-curvature grooves (one has a diameter of 160 mm and the other has a diameter of 80 mm). During the experiment, the continuum robot is placed into the template grooves, with the proposed strategy estimating the shape of these grooves. For each measurement, the location of the annular magnet is aligned to the start position of the constant-curvature arcs, with its direction kept vertical up. The position of the annular magnet is set as $\mathbf{p}_0 = [0, 0, 0]^\top$, with its magnetic moment set as $\mathbf{m}_c = [0, 0, 0.836]^\top$. Before the experiment, the background noises measured by the Hall-effect sensors and IMUs need to be cleared to eliminate the fabrication and assembly errors.

Firstly, we conduct a performance comparison of shape estimation for the continuum robot to select the optimal curve fitting method in the case where the continuum robot is placed in the constant-curvature groove with a diameter of 160 mm. The positions and orientations of three sensor modules are first obtained using the proposed localization approach, based on which three curve fitting methods are utilized for shape estimation of the continuum robot. The experimental results are presented in Fig. 5, showing that all three curves fitted by different methods have a good agreement with the curve for the ground truth. It can also be observed that the accuracy of the obtained sensor position decreases with the increase of the distance between the sensor and the magnet, which is quite reasonable since the magnetic fields generated by the magnet become weaker and the signal-to-noise ratio decreases as the distance increases. The shape estimation error is calculated as the Euclidean distance between two points on the fitting curve and the ground truth curve, respectively. The error

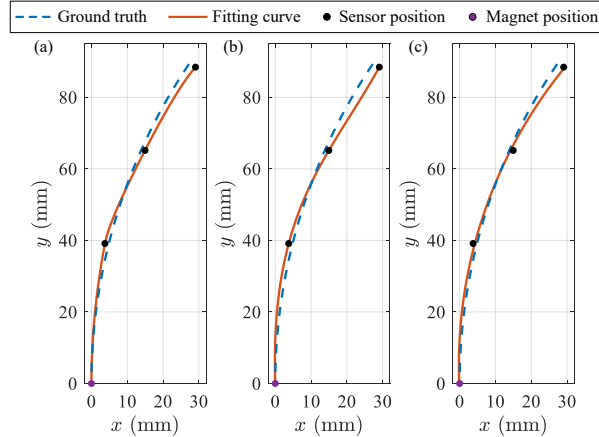


Fig. 5. Shape estimation using different curve fitting methods. (a) Piecewise quadratic Bezier curve fitting. (b) Cubic Bezier curve fitting. (c) Circular-arc curve fitting.

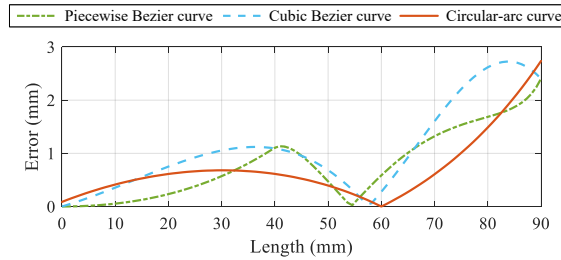


Fig. 6. Shape estimation using different curve fitting methods. (a) Piecewise quadratic Bezier curve fitting. (b) Cubic Bezier curve fitting. (c) Circular-arc curve fitting.

comparison is shown in Fig. 6, which indicates that the error of each fitting curve increases at the beginning and then drops to approximately zero, before increasing again till the end of the curve. The circular-arc curve presents the highest accuracy, with a mean absolute error (MAE) of about 0.70 mm, compared to the piecewise Bezier curve (MAE: 0.79 mm) and the cubic Bezier curve (MAE: 1.08 mm), which may because the Bezier curve needs to pass every sensor position with estimation errors while the circular-arc fitting curve employs the Kasa least-squares circle. The overall computational time of the sensor positioning and curve fitting process is around 40 ms, which presents a shape estimation frequency of about 25 Hz and could satisfy the real-time control requirement. Consequently, the circular-arc curve fitting method is selected for shape estimation of the continuum robot in the following test.

After that, the continuum robot is placed in these 3D-printed template grooves subsequently, with their shapes estimated by the sensor positioning approach and the circular-arc curve fitting method. The experimental results are

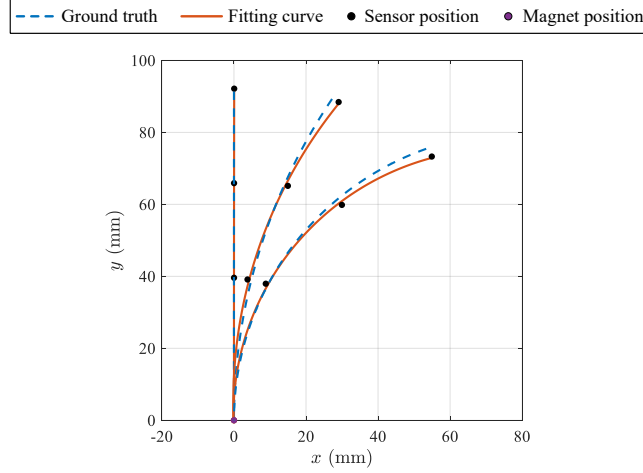


Fig. 7. Shape estimation using different curve fitting methods. (a) Piecewise quadratic Bezier curve fitting. (b) Cubic Bezier curve fitting. (c) Circular-arc curve fitting.

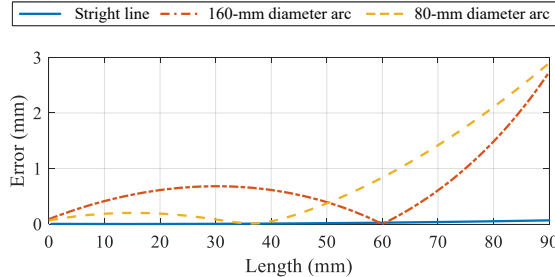


Fig. 8. Shape estimation using different curve fitting methods. (a) Piecewise quadratic Bezier curve fitting. (b) Cubic Bezier curve fitting. (c) Circular-arc curve fitting.

shown in Fig. 7, which demonstrate that our proposed strategy can achieve accurate shape estimation of these grooves. The estimation errors are shown in Fig. 8, with the MAE as 0.02 mm, 0.70 mm, and 0.84 mm for the straight groove, 160-mm diameter groove, and 80-mm diameter groove, respectively. Similarly, it can be observed that the sensor position errors increase with the increase of the distance between the sensor and magnet, and that the estimation errors increase at the proximal part and then drop to approximately zero before increasing again till the distal end of the continuum robot. The maximum estimation error is less than 3 mm ($\approx 3\%$) for the 90-mm length continuum robot, which is acceptable for most applications. The effectiveness and efficacy of the proposed shape estimation strategy using multiple Hall-effect sensors and IMUs are thus validated by these experimental results.

4 Conclusion

This work presents a novel real-time, low-cost, and high-accuracy shape estimation strategy for continuum robots based on synergistic fusion of embedded Hall-effect sensors and IMUs. The approach employs an annular magnet at the robot base to generate measurable magnetic fields, while sensor modules capture field vectors and orientation data. An optimization framework fusing magnetic field data and orientation data measured by the sensor module enables precise sensor localization, with the Kasa least-squares circular arc method proving superior for shape reconstruction. Experimental validation confirms sub-millimeter accuracy (less than 1 mm mean error) and robust real-time performance (25 Hz) across varying curvatures. The system achieves maximum errors below 3 mm without external infrastructure, outperforming single-sensor methods in confined environments. This framework provides a practical foundation for enhancing control precision in medical and industrial applications.

References

1. Webster III, R.J., Jones, B.A.: Design and kinematic modeling of constant curvature continuum robots: A review. *The International Journal of Robotics Research* **29**(13), 1661–1683 (2010)
2. Li, Y., Guo, C., Xin, W., Pan, T., Li, W., Chiu, P.W.Y., Li, Z.: Design and preliminary evaluation of an electromagnetically actuated soft-tethered colonoscope. *IEEE Transactions on Medical Robotics and Bionics* **3**(2), 402–413 (2021)
3. Huang, Y., Li, W., Zhang, X., Li, J., Li, Y., Sun, Y., Chiu, P.W.Y., Li, Z.: 4-dof visual servoing of a robotic flexible endoscope with a predefined-time convergent and noise-immune adaptive neural network. *IEEE/ASME Transactions on Mechatronics* **29**(1), 576–587 (2023)
4. Russo, M., Sadati, S.M.H., Dong, X., Mohammad, A., Walker, I.D., Bergeles, C., Xu, K., Axinte, D.A.: Continuum robots: An overview. *Advanced Intelligent Systems* **5**(5), 2200367 (2023)
5. Burgner-Kahrs, J., Rucker, D.C., Choset, H.: Continuum robots for medical applications: A survey. *IEEE transactions on robotics* **31**(6), 1261–1280 (2015)
6. Mahl, T., Hildebrandt, A., Sawodny, O.: A variable curvature continuum kinematics for kinematic control of the bionic handling assistant. *IEEE transactions on robotics* **30**(4), 935–949 (2014)
7. Wang, L., Simaan, N.: Geometric calibration of continuum robots: Joint space and equilibrium shape deviations. *IEEE Transactions on Robotics* **35**(2), 387–402 (2019)
8. Li, Y., Li, W., Xin, W., Zhang, X., Xian, Y., Chiu, P.W.Y., Li, Z.: Orientation control of an electromagnetically actuated soft-tethered colonoscope based on 2or pseudo-rigid-body model. In: 2021 IEEE International Conference on Robotics and Automation (ICRA). pp. 1191–1197. IEEE (2021)
9. Shi, C., Luo, X., Qi, P., Li, T., Song, S., Najdovski, Z., Fukuda, T., Ren, H.: Shape sensing techniques for continuum robots in minimally invasive surgery: A survey. *IEEE Transactions on Biomedical Engineering* **64**(8), 1665–1678 (2016)
10. Huang, X., Zou, J., Gu, G.: Kinematic modeling and control of variaible curvature soft continuum robots. *IEEE/ASME Transactions on Mechatronics* **26**(6), 3175–3185 (2021)

11. Song, S., Li, Z., Yu, H., Ren, H.: Electromagnetic positioning for tip tracking and shape sensing of flexible robots. *IEEE Sensors Journal* **15**(8), 4565–4575 (2015)
12. Ma, X., Chiu, P.W.Y., Li, Z.: Shape sensing of flexible manipulators with visual occlusion based on bezier curve. *IEEE Sensors Journal* **18**(19), 8133–8142 (2018)
13. Boctor, E.M., Choti, M.A., Burdette, E.C., Webster Iii, R.J.: Three-dimensional ultrasound-guided robotic needle placement: an experimental evaluation. *The International Journal of Medical Robotics and Computer Assisted Surgery* **4**(2), 180–191 (2008)
14. Lobaton, E.J., Fu, J., Torres, L.G., Alterovitz, R.: Continuous shape estimation of continuum robots using x-ray images. In: 2013 IEEE international conference on robotics and automation. pp. 725–732. IEEE (2013)
15. Monet, F., Sefati, S., Lorre, P., Poiffaut, A., Kadoury, S., Armand, M., Iordachita, I., Kashyap, R.: High-resolution optical fiber shape sensing of continuum robots: A comparative study. In: 2020 IEEE international conference on robotics and automation (ICRA). pp. 8877–8883. IEEE (2020)
16. Wang, F., Jiang, Q., Li, J.: Shape sensing for continuum robots using fbg sensors array considering bending and twisting. *IEEE Sensors Journal* **24**(2), 1546–1554 (2023)
17. Hou, L., Zhao, X., Chen, T., Zhang, Y., Ling, Q., Tao, B.: A sensing strategy combining kinematic model with fbg sensors for continuum robots. *IEEE Transactions on Instrumentation and Measurement* (2025)
18. Cheng, H., Xu, H., Shang, H., Wang, X., Liu, H., Liang, B.: Orientation to pose: Continuum robots shape reconstruction based on the multi-attitude solving approach. In: 2022 International Conference on Robotics and Automation (ICRA). pp. 3203–3209. IEEE (2022)
19. Sofla, M.S., Sadigh, M.J., Zareinejad, M.: Shape estimation of a large workspace continuum manipulator with fusion of inertial sensors. *Mechatronics* **80**, 102684 (2021)
20. Peng, R., Wang, Y., Lu, P.: A tendon-driven continuum manipulator with robust shape estimation by multiple imus. *IEEE Robotics and Automation Letters* **9**(4), 3084–3091 (2024)
21. Guo, H., Ju, F., Cao, Y., Qi, F., Bai, D., Wang, Y., Chen, B.: Continuum robot shape estimation using permanent magnets and magnetic sensors. *Sensors and Actuators A: Physical* **285**, 519–530 (2019)
22. Pittiglio, G., Donder, A., Dupont, P.E.: Continuum robot shape estimation using magnetic ball chains. In: 2024 IEEE/RSJ International Conference on Intelligent Robots and Systems (IROS). pp. 11004–11009. IEEE (2024)
23. Zhao, Q., Lai, J., Huang, K., Hu, X., Chu, H.K.: Shape estimation and control of a soft continuum robot under external payloads. *IEEE/ASME Transactions on Mechatronics* **27**(5), 2511–2522 (2021)
24. Thuruthel, T.G., Shih, B., Laschi, C., Tolley, M.T.: Soft robot perception using embedded soft sensors and recurrent neural networks. *Science Robotics* **4**(26), eaav1488 (2019)
25. Abbott, J.J., et al.: Magnetic methods in robotics. *Annu. Rev. Control Robot.* **3**, 57–90 (2020)
26. Baydas, S., Karakas, B.: Defining a curve as a bezier curve. *Journal of Taibah University for Science* **13**(1), 522–528 (2019)
27. Kåsa, I.: A circle fitting procedure and its error analysis. *IEEE Transactions on Instrumentation and Measurement* **IM-25**(1), 8–14 (1976)